Journal of
Materials Chemistry C

ROYAL SOCIETY
OF CHEMISTRY

PAPER

View Article Online
View Journal | View Issue

Check for updates

Cite this: *J. Mater. Chem. C*, 2023, **11**, 16806

Understanding the role of Tris(2-aminoethyl)amine in stabilizing mixed-cation perovskites under humid and thermal stress conditions†

Priyanka Chhillar, Amit Kumar, Bhanu Pratap Dhamaniya,‡ Kartiki Chandratre, Saurabh Pareek, Sandeep Kumar Pathak and Supravat Karak *

Received 26th July 2023,
Accepted 18th November 2023

DOI: 10.1039/d3tc02644b

rsc.li/materials-c

Mixed organic–inorganic lead halide perovskites have emerged as promising optoelectronic materials for photovoltaic applications in the span of a few years. Mixed cation $FA_{1-x}Cs_x$ perovskites have been widely explored as a resolution to the phase instability issue in $FAPbI_3$ and $CsPbI_3$ perovskites. In this study, the impact of Tris(2-aminoethyl)amine (TAEA) on $FA_{0.83}Cs_{0.17}Pb(I_{0.90}Br_{0.10})_3$ absorber layer stability under humid and thermal stress conditions has been investigated. Interestingly, the incorporation of TAEA in the perovskite precursor has resulted in enhanced structural and optoelectronic properties. Moreover, TAEA addition has led to greatly enhanced thermal and ambient stability. TAEA containing $FA_{0.83}Cs_{0.17}Pb(I_{0.90}Br_{0.10})_3$ films retained their black phase even after 180 days of exposure to a highly humid environment with RH ~ 60–70% and more than 7 days on exposure to continuous thermal stress at 85 °C along with high humidity and illumination. Therefore, the perovskite films fabricated with the optimized concentration of TAEA in $FA_{0.83}Cs_{0.17}Pb(I_{0.90}Br_{0.10})_3$ perovskite have great potential for application in high performance devices with excellent thermal and ambient stability.

Introduction

In the past decade, organic–inorganic lead halide perovskites have turned out to be a cost-efficient and promising alternative photovoltaic technology due to their excellent semiconductor properties such as tunable bandgap across a wide range, large charge carrier diffusion lengths ($\sim 1\ \mu m$), low exciton binding energies and large absorption coefficients (10^4 to $10^5\ cm^{-1}$) in the solar spectrum region.[1–3] Within a few years of development, a record power conversion efficiency of 25.8% has been attained in perovskite solar cells.[4] Methylammonium lead iodide ($MAPbI_3$) was the initial perovskite composition that was studied widely and several other perovskite material compositions have also been studied to date owing to the poor stability of $MAPbI_3$ perovskite material. In $MAPbI_3$ the organic MA part is highly hygroscopic and also thermally unstable, preventing the widespread commercialization of this material.[5–8] $MAPbI_3$ easily dissociates into CH_3NH_2, HI, and PbI_2 on exposure to moisture.[9,10]

Therefore, formamidinium lead iodide [$FAPbI_3$, $HC(NH_2)_2PbI_3$] has been investigated as an alternative light harvesting perovskite material in most of the high-performance photovoltaic devices due to its superior thermal and photo-stability and favorable band gap of 1.47 eV.[11,12] However, $FAPbI_3$ suffers from phase transition from the black photoactive α-$FAPbI_3$ phase which is stable only above 150 °C to the yellow non-photoactive hexagonal phase δ-$FAPbI_3$ at room temperature and in a humid atmosphere.[13,14] Various approaches have been formulated for stabilization of the α-$FAPbI_3$ phase by mixing an amount of MAI into $FAPbI_3$.[15,16] However, this mixed-organic cation perovskite composition ($MA_xFA_{1-x}PbI_3$) might not attain thermal and ambient stability due to the presence of a volatile organic part.[17] So, as an alternative researchers have followed various approaches to stabilize the α-$FAPbI_3$ phase by using inorganic monovalent cations such as Cs^+, K^+, or Rb^+, ensuring improved stability and device performance.[18–24] Although there are various studies employing mixed multiple cations such as FAMACs,[20] FAMACsRb,[20,25] or FAMACsK[20] to stabilize the photoactive phase, however, the presence of volatile MA components makes them susceptible to instability at high temperatures.[26] Therefore, MA-free FA-Cs mixed-cation perovskite films need to be developed and investigated.

It is reported that the optimum concentration of Cs in $FA_{1-x}Cs_x$ has to be in the range $0.10 < x < 0.20$, for which the Goldschmidt tolerance factor is also within the range to

---

Department of Energy Science and Engineering, Indian Institute of Technology Delhi, Hauz Khas, New Delhi-110016, India. E-mail: supravat@dese.iitd.ac.in

† Electronic supplementary information (ESI) available. See DOI: https://doi.org/10.1039/d3tc02644b

‡ Present address: U.R.Rao Satellite Centre, Indian Space Research Organisation, Bengaluru 560017, Karnataka, India.

form a stable perovskite structure and thus preferred to form a black α-$FAPbI_3$ phase. However, when the content of Cs ions is increased to higher values of up to 30%, the appearance of a diffraction peak corresponding to α-$CsPbI_3$ is noticed.[27] α-$CsPbI_3$ which is a photoactive phase is stable only at temperatures above 320 °C and transforms to the photoactive γ-$CsPbI_3$ phase when quenched to room temperature in an inert atmosphere.[28–34] However, α-$CsPbI_3$ transforms abruptly to the non-photoactive δ-$CsPbI_3$ on exposure to atmospheric moisture.[22,35,36] Therefore, α-$CsPbI_3$ is more sensitive to atmospheric moisture, which renders it unsuitable for photovoltaic applications.[37,38] $FA_{0.83}Cs_{0.17}PbX_3$ perovskite composition is widely studied and employed as an absorber layer in solar cells.[39–42]

In this study, we have explored the effect of Tris(2-aminoethyl)amine (TAEA) on the thermal and moisture stability of MA-free mixed-cation perovskite compositions $FA_{0.83}Cs_{0.17}Pb(I_{0.90}Br_{0.10})_3$. The effect of different concentrations of TAEA added in $FA_{0.83}Cs_{0.17}Pb(I_{0.90}Br_{0.10})_3$ precursor was studied extensively to find the optimum composition. Addition of TAEA in $FA_{0.83}Cs_{0.17}Pb(I_{0.90}Br_{0.10})_3$ leads to an enhancement in the absorbance and optoelectronic properties of the host perovskite material. XRD measurements were conducted to explore the degradation of perovskite film under thermal stress and a highly humid ambient environment. TAEA incorporation has resulted in greatly enhanced ambient and thermal stability. XPS and FTIR measurements were carried out to examine the interaction of TAEA with $FA_{0.83}Cs_{0.17}Pb(I_{0.90}Br_{0.10})_3$ perovskite crystal lattice. This work provides insights into designing a long-term stable double cation perovskite composition for photovoltaic applications.

Results and discussion

XRD patterns were recorded to study the impact of introducing different amounts of TAEA in $FA_{0.83}Cs_{0.17}Pb(I_{0.90}Br_{0.10})_3$ (denoted as FACs from hereon) perovskite as shown in Fig. 1a. Characteristic peaks at 2θ values 14.02°, 19.94°, 24.44°, 28.34°, 31.76°, 34.82°, 40.46°, and 43.06° which correspond to the (001), (011), (111), (002), (012), (112), (022), and (033) planes respectively are detected in all the perovskite films corresponding to the photoactive α-$FAPbI_3$ phase.[43] XRD analysis confirmed that all the films crystallize into the α-phase irrespective of the concentration of added TAEA. Also, no additional peak was observed in any of the TAEA-containing films towards the low 2θ values signifying the absence of any 2D phase formation.

With the increase in the concentration of TAEA, an enhancement in the XRD peak intensity is noticed until the concentration where 1 μL of TAEA is added into 200 μL of the FACs precursor, and beyond this the peak intensity is almost similar to the control FACs film. This confirms that the addition of TAEA leads to an improvement in the crystallinity of the FACs films. Fig. 1b shows the individual XRD peak shift in peaks at around 2θ values 14°, 20°, and 28°. With the incorporation of TAEA in FACs perovskite the XRD peaks shift towards higher 2θ values which confirms the presence of TAEA.

Absorption spectra were recorded to assess the impact of the incorporation of TAEA in FACs perovskite on the absorbance properties. An absorption profile with an absorption edge at around 780 nm corresponding to a bandgap of around 1.6 eV is detected for all the films. The UV-Vis absorption spectra shown in Fig. 2a show an increase in the absorbance with the addition of TAEA in FACs perovskite. The maximum absorbance is observed for the FACs perovskite film containing 1 μL of TAEA in 200 μL of perovskite precursor. Fig. 2b shows the corresponding Tauc plots of the UV-Vis spectra shown in Fig. 2a. It is observed that with the increase in the TAEA concentration, there is a very slight increase in the bandgap of the perovskite from 1.590 to 1.616 eV.

Steady-state photoluminescence (PL) was recorded to observe the effect of TAEA addition on the optoelectronic properties of the FACs perovskite. An increase in the PL intensity is observed with the incorporation of TAEA when compared with the control film as shown in Fig. 2c. All the TAEA containing films show better photoluminescence than the pristine FACs film, indicating a great reduction in the defect-mediated non-radiative recombination. In accordance with the increase in the crystallinity of the film as noticed from the XRD spectra, the PL intensity also increases with the increase in the concentration of TAEA in perovskite precursor until reaching a concentration where 1 μL of TAEA is added into 200 μL of precursor. However, beyond this concentration, the PL intensity starts to decrease. So, as evident from the XRD analysis, UV-Vis absorption spectra and PL spectra the optimum concentration of TAEA in the FACs precursor is considered to be 1 μL in 200 μL, respectively. Normalized PL is plotted as shown in Fig. 2d to examine the peak shift with the incorporation of TAEA. There is a negligible blue shift in the peak position of the order of ~1–2 nm which is in accordance with the aforementioned very slight increase in the bandgap detected from the UV-Vis absorption spectra.

The size of TAEA is large as compared to FA and Cs, therefore it is less likely that it will substitute the A-site cations in the FACs perovskite lattice. Additionally, there is no sign of 2D phase formation from the XRD, UV-Vis, and PL studies. There are no low angle peaks observed in the XRD patterns with 2θ less than 10°, which carries the signature of 2D phase formation.[44,45] Additionally, the single PL peak and lack of any excitonic peak in the UV-Vis spectra clearly hint towards the absence of a 2D phase.[45–47] So, most likely the TAEA is present on the surface of the perovskite. Therefore, the shift in the XRD peaks towards higher 2θ values can possibly be caused by the compressive strain present in the TAEA containing films. The strain could be induced due to the interaction of TAEA with the perovskite lattice during or after crystallization, introduced distortions in the octahedral environment surrounding the metal cations (Pb). The presence of TAEA on the surface of the perovskite crystals may affect the local atomic arrangement and crystal symmetry, causing shifts in the XRD peaks. Therefore, we have carried out Williamson–Hall analysis to calculate the strain from XRD patterns and the calculated strain is plotted below in Fig. S1 (ESI†). The plot shows an increase in

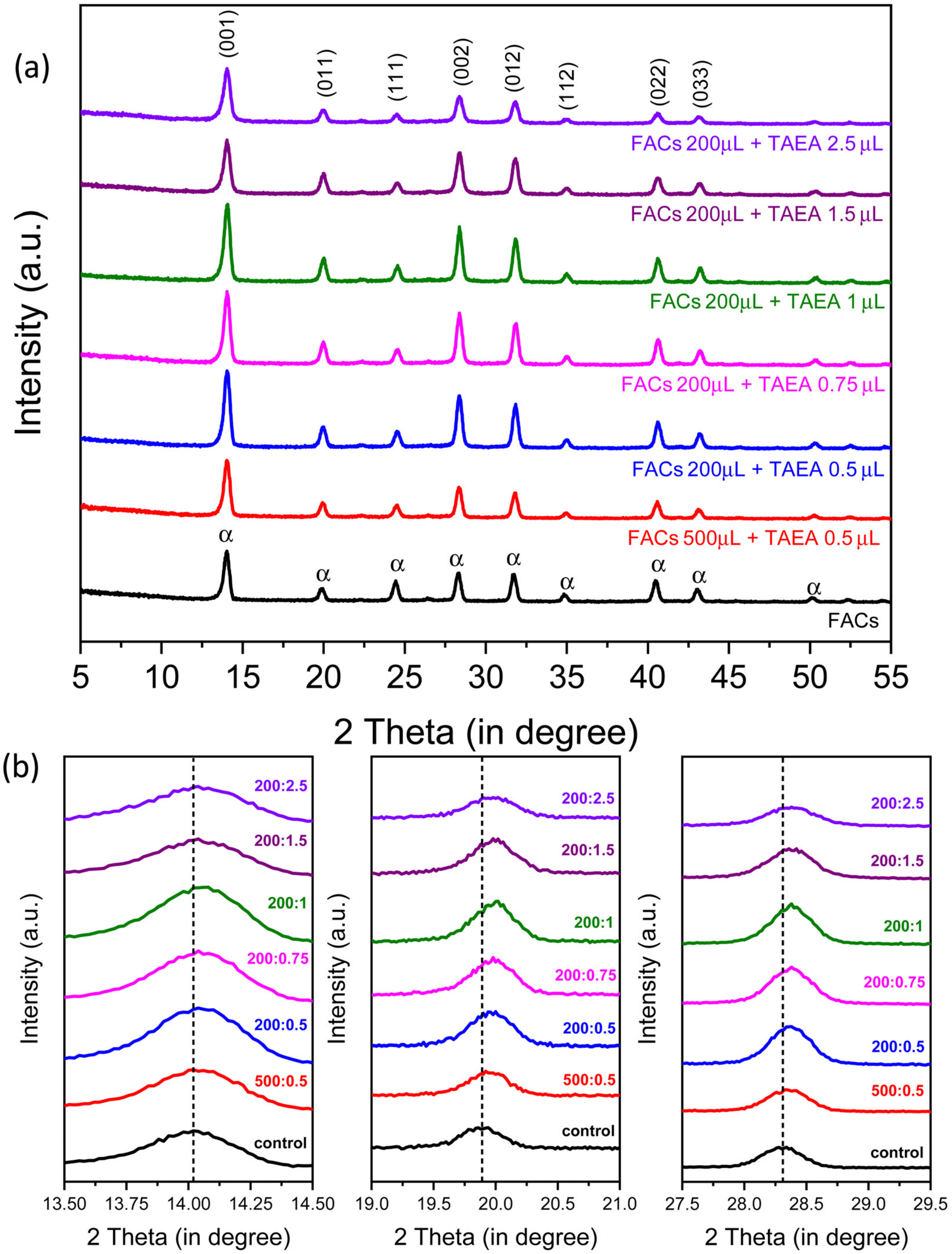

Fig. 1 Crystallography analysis of $FA_{0.83}Cs_{0.17}Pb(I_{0.90}Br_{0.10})_3$ thin film. (a) XRD for $FA_{0.83}Cs_{0.17}Pb(I_{0.90}Br_{0.10})_3$ film containing different concentrations of TAEA added inside perovskite precursor. (b) XRD peak shift for 2θ around 14°, 20°, and 28° for TAEA containing films with different concentrations of TAEA added in $FA_{0.83}Cs_{0.17}Pb(I_{0.90}Br_{0.10})_3$ perovskite precursor.

the microstrain with an increase in the concentration of TAEA in the FACs precursor.

The impact of TAEA addition on the FACs film morphology was observed using field emission scanning electron microscopy (FESEM) and is presented in Fig. 3. Fig. 3a and b show the morphology of the fresh FACs film with high and low magnifications, respectively. The FACs film shows a rough morphology with a lot of large pinholes in the order of a few μm as shown in the low magnification image, which could be detrimental to the device performance. This could be the reason for the aforementioned lowest PL intensity observed in the FACs film. As TAEA is added inside the precursor of FACs the pinholes start to decrease as shown in Fig. 3d, f and h until the concentration where 0.75 μL of TAEA is added into 200 μL of perovskite precursor. When the concentration of TAEA is further increased to 1 μL per 200 μL of FACs precursor, the

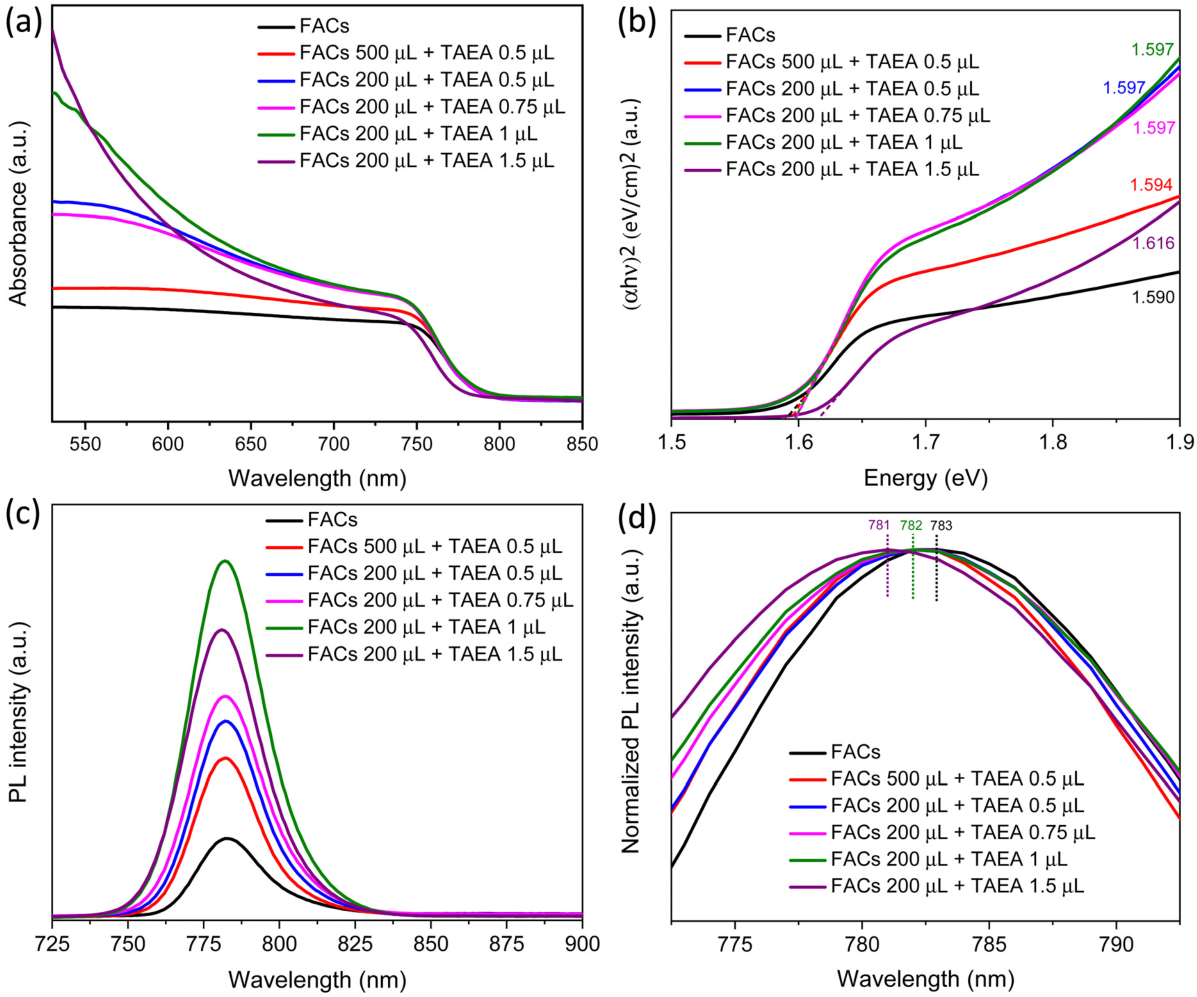

Fig. 2 UV-Vis absorption and PL spectra. (a) UV-Vis absorption spectra and (b) Tauc plot for FACs films with different concentrations of TAEA added in perovskite precursor. (c) PL spectra and (d) a normalized PL plot for FACs films with different concentrations of TAEA added in perovskite precursor.

pinholes are completely removed and we obtain a uniform and compact film. However, with a further increase in the concentration of TAEA the pinholes reappear as shown in Fig. 3l. This could possibly be the reason for the aforementioned highest PL observed in the 1 μL TAEA concentration which starts reducing with a further increase in TAEA concentration.

It is also observed from the high magnification images presented in Fig. 3a, c, e, g, i and k that the grain size is reduced with the incorporation of TAEA. Micro-strain induced by introducing TAEA could have resulted in the reduced crystallite size. Additionally, the films become more compact and smoother with the increase in the concentration of TAEA. This could be ascertained from the atomic force microscopy (AFM) images shown in Fig. 4. The 2D and 3D AFM images confirm that the incorporation of TAEA leads to smoothening of the films as the root mean square roughness (R_{rms}) is reduced with the increase in the concentration of TAEA. The lowest R_{rms} = 58.47 nm is detected in the film containing 1 μL of TAEA per 200 μL of FACs precursor, which is increased to a value of 61.72 nm on further increase in TAEA concentration. So, from FESEM and AFM it is witnessed that the film containing 1 μL of TAEA per 200 μL of FACs precursor renders a smooth, uniform, compact, and pinhole free film, which is critical for efficient planar heterojunction-devices.

Scanning laser confocal microscopy (SLCM) was also performed to examine the spatial distribution of luminescence intensity. Images in Fig. 5a–f represent the luminescence maps of the FACs films with different concentrations of TAEA. The pristine FACs film is shown to have a number of dark spots which depict the non-radiative emission sites. These dark spots mainly represent the defect sites at grain boundaries and the pinholes in the film as observed from the FESEM image in Fig. 3b. Additionally, the fluorescence density of 1.71×10^6 which is calculated over an area of 16384 μm^2 in pristine FACs film is also the lowest among all the films as presented in Fig. 5g. With the addition of a small amount of TAEA in FACs (0.5 μL in 200 μL) the black spots are significantly reduced as can be seen from Fig. 5b and consequently there is an increase in the fluorescence density (= 1.95×10^6) as well. Moreover, a further increase in the concentration of TAEA in FACs precursor leads to greatly reduced black spots, and the fluorescence density is increased to a value of 2.09×10^6. This is in

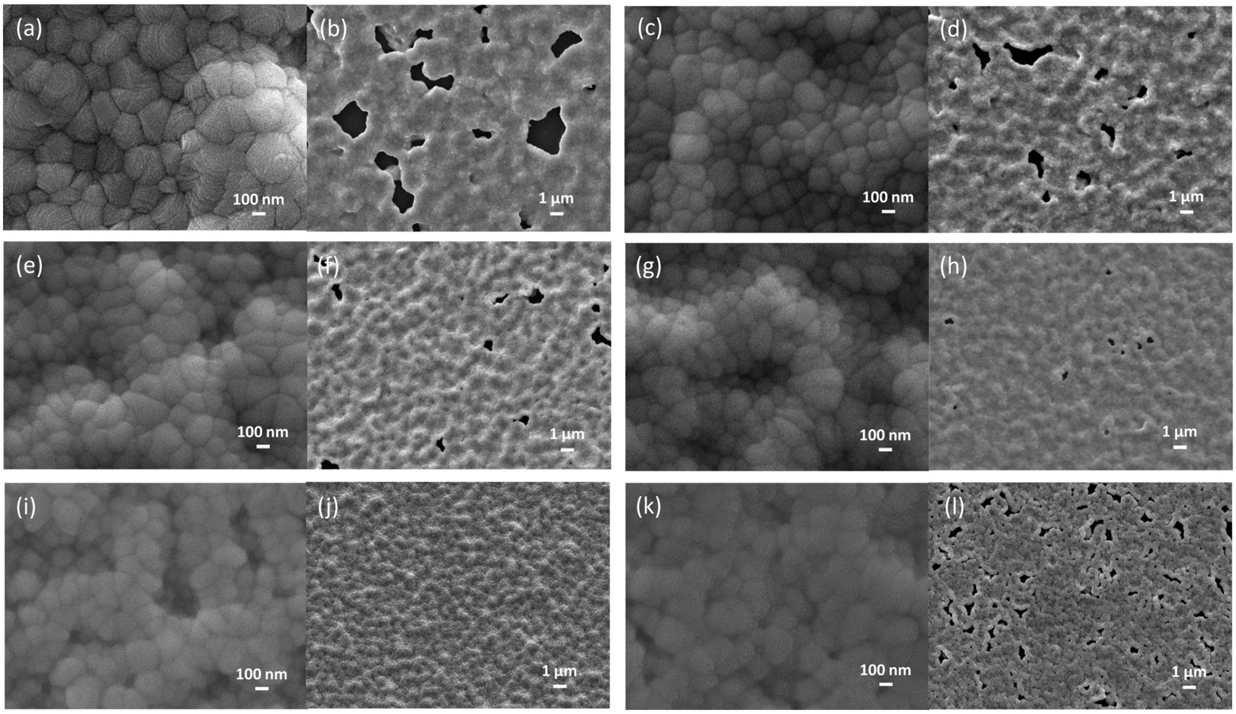

Fig. 3 FESEM morphology of fresh FACs film (a) high magnification (50k×), (b) low magnification (5k×); FACs film with TAEA with a volumetric concentration 500 : 0.5 (c) high magnification, (d) low magnification; FACs film with TAEA with a volumetric concentration 200 : 0.5 (e) high magnification, (f) low magnification; FACs film with TAEA with a volumetric concentration 200 : 0.75 (g) high magnification, (h) low magnification; FACs film with TAEA with a volumetric concentration 200 : 1 (i) high magnification, (j) low magnification; FACs film with TAEA with a volumetric concentration 200 : 1.5 (k) high magnification, and (l) low magnification.

agreement with the aforementioned increase in steady-state PL intensity and reduction in the pinholes with the increase in the concentration of TAEA as depicted in Fig. 2c and 3.

The film with 1 μL in 200 μL of FACs shows the most uniform and brightest emission distribution among the other compositions without any visible pinholes, consistent with the PL data shown in Fig. 2c. This film shows the highest fluorescence density of 2.41×10^6 among all the films. The observation from the spatial PL is consistent with previous observations and this is the optimum composition showcasing the best structural, morphological, and optoelectronic properties. Further increase in the TAEA concentration leads to the reappearance of black spots and reduced fluorescence density ($= 2.13 \times 10^6$), as observed from Fig. 5f and g.

To assess the heterogeneity of PL emission across the sample, a line profile was plotted across the breadth of the film as depicted by the white line in Fig. 5a–f. The FACs film shows the most inhomogeneous distribution of PL intensity

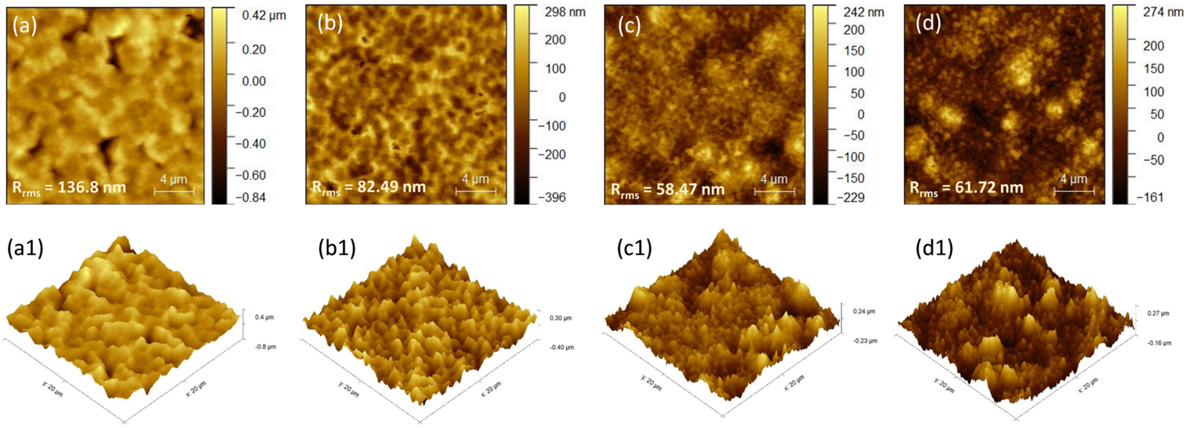

Fig. 4 AFM images. (a) 2D and (a1) 3D AFM topography images of FACs film, (b) 2D and (b1) 3D AFM topography images of FACs film with TAEA with a volumetric concentration of 200 : 0.5, (c) 2D and (c1) 3D AFM topography images of FACs film with TAEA with a volumetric concentration of 200 : 1, and (d) 2D and (d1) 3D AFM topography images of FACs film with TAEA with a volumetric concentration of 200 : 1.5.

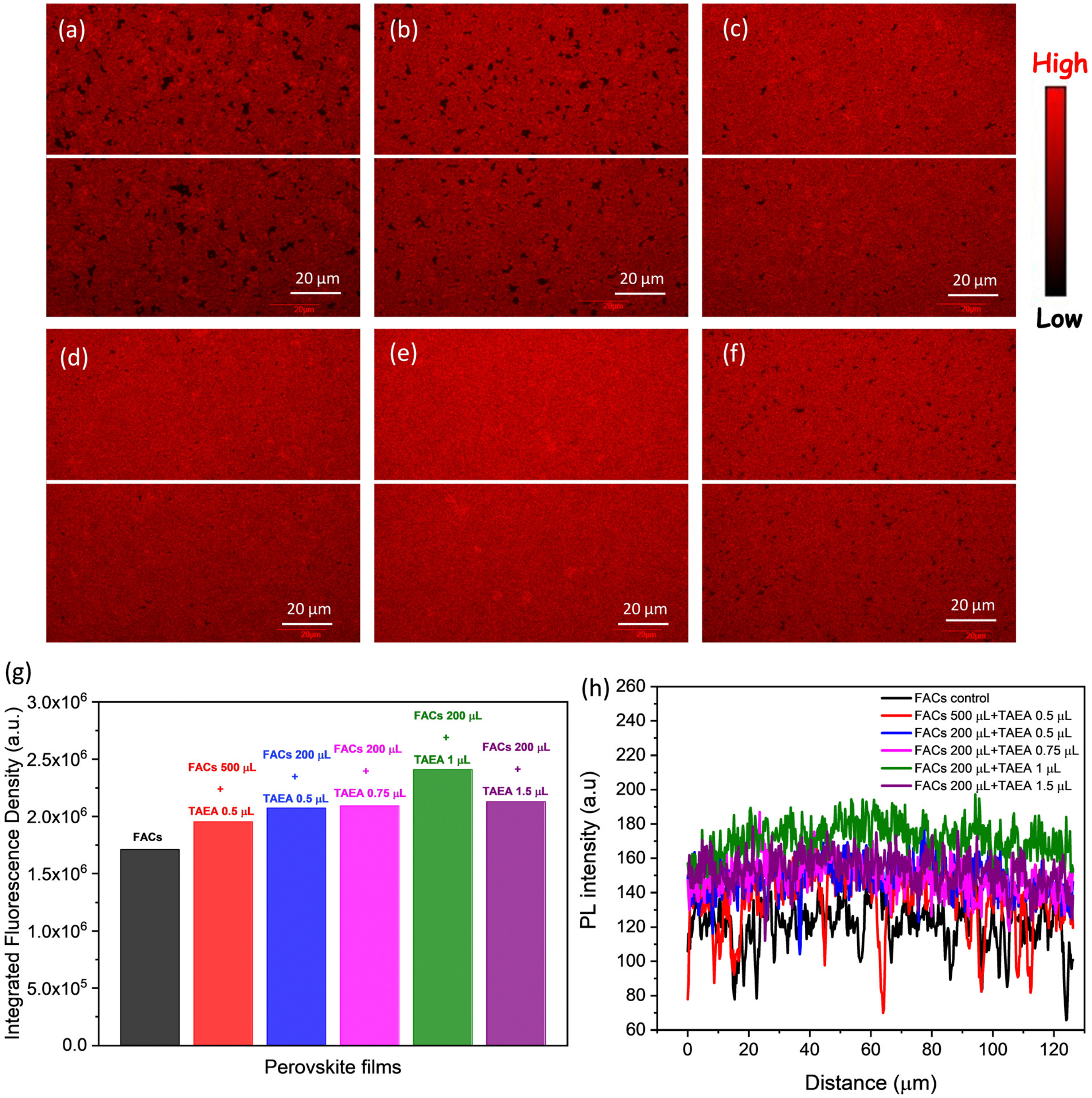

Fig. 5 SLCM PL intensity maps of (a) FACs film, FACs film containing (b) 0.5 µL of TAEA in 500 µL of FACs precursor, (c) 0.5 µL of TAEA in 200 µL of FACs precursor, (d) 0.75 µL of TAEA in 200 µL of FACs precursor, (e) 1 µL of TAEA in 200 µL of FACs precursor, and (f) 1.5 µL of TAEA in 200 µL of FACs precursor. (g) Integrated fluorescence density in the films calculated in the 128 µm × 128 µm area of the sample. (h) PL line profile plotted along the breadth of the samples as denoted by the white horizontal lines in (a)–(f).

across the sample with a lot of dips and showcases the lowest PL intensity. With the increase in the concentration of TAEA in the precursor, the PL intensity becomes more homogeneous and the overall PL intensity across the film is increased. Inspiringly, the highest PL intensity across the film is detected for the film with 1 µL of TAEA in 200 µL of FACs precursor, which is consistent with the aforementioned observations.

To understand the degradation of perovskite solar cells and find failures, stability testing under enhanced environmental stressing conditions such as high humidity, elevated temperature, and illumination becomes crucial. Therefore, all the films were kept outside under ambient temperature with RH ~ 60–70% to assess the impact of TAEA on the stability of the FACs films. Digital photographs of the films with time are presented in Fig. 6a. All the fresh films are initially found to be blackish in color, indicating the crystallization of films in the photoactive α-phase. The pristine FACs film started turning yellow towards the edges and corners after 110 days of exposure to the ambient environment and after 150 days a major portion of the film had turned yellow. However, all the FACs films containing different TAEA concentrations show a stable photoactive phase even after 180 days of exposure to light and highly humid conditions.

The XRD patterns of the FACs film and the optimized FACs film containing 1 µL of TAEA are presented in Fig. S2 (ESI†).

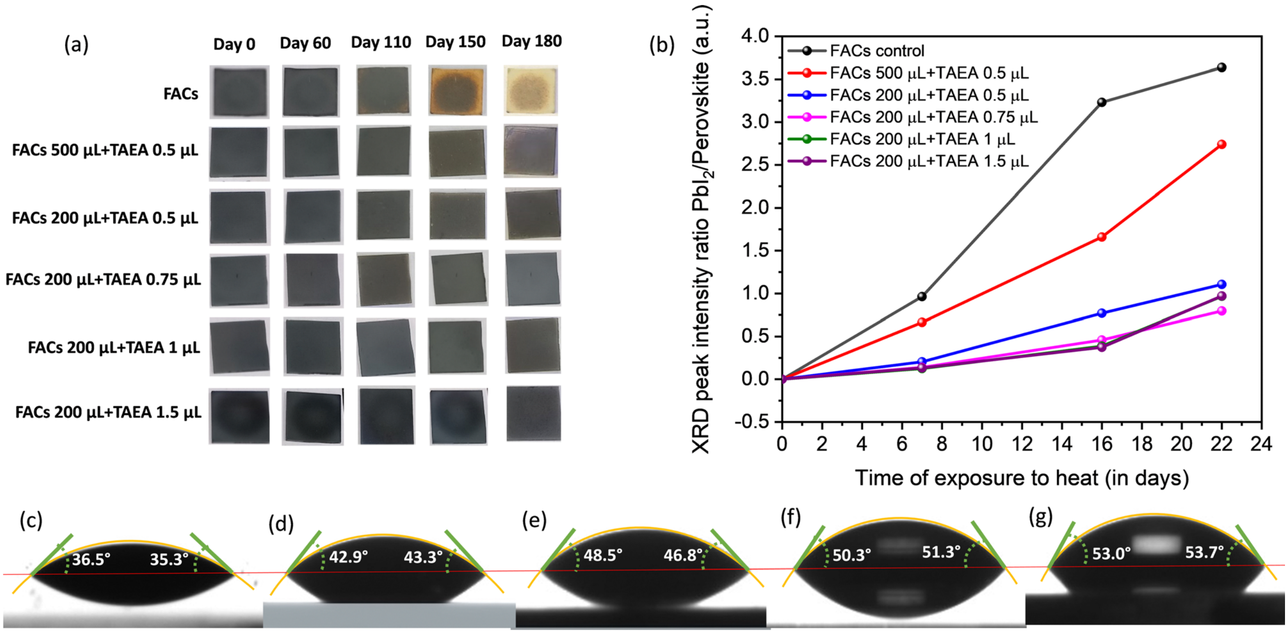

Fig. 6 (a) Digital photographs of FACs films with different concentrations of TAEA upon exposure to an ambient atmosphere with RH ∼ 60–70%. (b) XRD peak intensity ratio of PbI_2/perovskite *versus* time of exposure plot for FACs films with different concentrations of TAEA exposed to continuous heat at 85 °C in ambient atmosphere. Contact angle measurement for (c) the FACs film, and the FACs film containing (d) 0.5 μL of TAEA in 500 μL of FACs precursor, (e) 0.5 μL of TAEA in 200 μL of FACs precursor, (f) 1 μL of TAEA in 200 μL of FACs precursor, and (g) 1.5 μL of TAEA in 200 μL of FACs precursor.

It is clearly evident from the XRD pattern that both the films retain the initial α-phase until 60 days of exposure to ambient conditions. However, the pristine FACs film started degrading after 110 days as can be ascertained from the appearance of peaks corresponding to PbI_2, δ-$FAPbI_3$, and δ-$CsPbI_3$ at 2θ values ≈ 12.9°, 11.2°, and 9.86°, respectively. Whereas, the TAEA-containing film retains the α-$FAPbI_3$ phase even after 110 days of exposure to light and highly humid conditions, which is in accordance with the physical appearance of the films in terms of no color change noticed as shown in Fig. 6a. It is observed that the UV-Vis absorption spectra shown in Fig. S3 (ESI†) show a negligible decrease in the absorbance of the TAEA-containing films even after 110 days of exposure to RH ∼ 60–70%. This ascertains the fact that the film retains the initial perovskite phase even after exposure to highly humid conditions.

Water contact angle measurement was carried out to explore the surface wetting properties of the FACs films with different concentrations of TAEA as shown in Fig. 6c–g. With an increase in the concentration of TAEA the contact angle is increased signifying the decrease in the affinity to water with increasing amounts of TAEA. So, it is evident from the observations that the greater the amount of TAEA in the precursor the more the film surface is resistant to water ingress due to the presence of alkyl chains in TAEA. This explicates the reason for the higher ambient stability achieved in the TAEA containing films when compared to the pristine FACs film.

Apart from ambient stability, thermal stability is also crucial and one of the most challenging parameters for perovskite materials to survive. Hence, all the films were kept at continuous heat at 85 °C in an ambient environment with high humidity RH ∼ 60–70% to explore the thermal stability. XRD patterns were recorded at different intervals of time to assess the amount of degradation and the impact on the structural properties upon exposure to heat, as presented in Fig. S4 (ESI†). It is observed that after 7 days of continuous exposure to the ambience and heat the pristine FACs film shows the appearance of a diffraction peak corresponding to PbI_2 which is of almost equal intensity as that of the main (001) perovskite peak as shown in Fig. S4a (ESI†). However, as we keep increasing the amount of TAEA in the FACs films the intensity of the PbI_2 peak compared to the (001) perovskite peak keeps reducing and it is almost negligible for higher concentrations of TAEA starting from 0.75 μL of TAEA in 200 μL of FACs precursor. This can be clearly visualized from the ratio of PbI_2/perovskite XRD peak intensity *versus* the time plot shown in Fig. 6b. After 16 days of exposure to heat and humidity, two low intensity peaks pertaining to δ-$FAPbI_3$ and δ-$CsPbI_3$ start to appear along with the PbI_2 peak in the pristine FACs film, whose intensity has increased over further heating past this time. However in the TAEA containing films these peaks are absent even after 22 days of continuous heating. These observations clearly signify that the presence of TAEA in the FACs films has a remarkable effect on slowing down the degradation process in the presence of both heat and high humidity. Additionally, the incorporation of TAEA has also resulted in resisting the α → δ phase transition in the perovskite for a much longer duration, which is the biggest limitation in FA and Cs based perovskite materials.

X-ray photoelectron spectroscopy (XPS) studies were carried out as presented in Fig. 7, to gain insight into the chemical composition of FACs perovskite films with and without TAEA. The two Pb^{2+} 4f peaks are detected at binding energies (BEs) of 142.9 and 138 eV for the pristine FACs film which can be

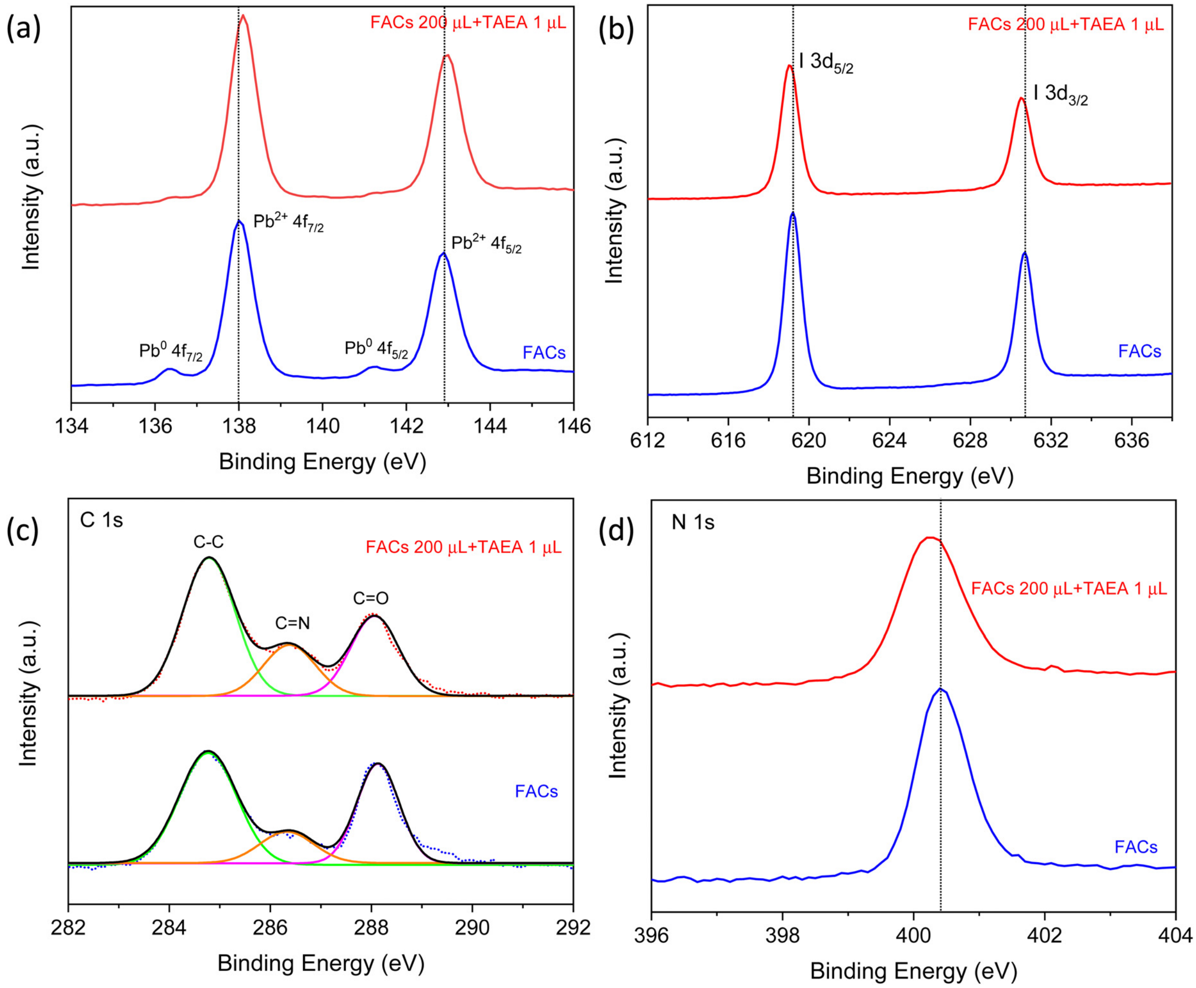

Fig. 7 XPS spectra of (a) Pb 4f, (b) I 3d, (c) C 1s, and (d) N 1s for FACs perovskite films with and without TAEA.

assigned to $4f_{5/2}$ and $4f_{7/2}$ core levels as shown in Fig. 7a. Along with these, two weak shoulder peaks at lower BEs of 141.3 and 136.3 eV are also detected that correspond to the metallic Pb^0 4f. Metallic lead (Pb^0) is detrimental to device performance as its presence indicates the presence of defect sites, resulting in non-radiative recombination.[48,49] Pb^0 reflects the presence of iodide and cation vacancies in the perovskite. With the addition of TAEA, there is a shift of the Pb^{2+} peaks towards higher BEs and the Pb^0 peak intensity has reduced to almost negligible magnitude. This shows that the TAEA incorporation is affecting the chemical environment of the Pb and also inhibiting the defects, hence contributing to the greatly decreased Pb^0 peak.

The peaks at 630.7 and 619.2 eV in the pristine FACs films are associated with I $3d_{3/2}$ and I $3d_{5/2}$, respectively, as shown in Fig. 7b. The addition of TAEA results in the shifting of these peaks towards lower BEs indicating the interaction of I^- with TAEA. It is previously reported that an organic additive containing $-NH_2$ can form a N–H···X H-bond with the halide ions and hence helps in restricting the migration of halide ions pertaining to the ionic nature of perovskites.[50] This suppression of the migration of I^- results in reducing the iodide defects and enhancing the hydrophobicity of perovskite.

The BEs in C 1s XPS spectra at 284.8, and 286.4 eV as presented in Fig. 7c are assigned to the C–C, $C{=}NH^{2+}$, respectively from FA^+. The peak at 288 eV corresponds to C═O, which reflects the degradation of perovskite film on exposure to the ambient environment.[39] The peak area of C═O visibly decreases with the addition of TAEA which implies that the target film is more resistant to H_2O or O_2 and hence exhibits improved film stability. The N 1s peak at BE 400.4 eV shifts slightly towards the lower BE value of 400.3 eV, indicating that the BE of N in FA is affected by the interaction of TAEA with the lattice as shown in Fig. 7d.

Amine additives are shown to be capable of modulating the crystallization process. TAEA can coordinate with the metal cations present in the perovskite structure such as Pb^{2+} through its amino groups, which can act as ligands to form coordination bonds with the metal cations. This facilitates a better nucleation and crystallization process and leads to the formation of well-ordered and more crystalline films. The amino groups in TAEA can also bind to the undercoordinated surface Pb ions in the perovskite, forming coordination bonds.[51–53] TAEA can passivate the crystallographic defect and trap states present on the surface of perovskite films, reducing the non-radiative recombination and improving the overall optical and electronic properties of the perovskite material. This enhanced surface passivation prevents the formation of unwanted surface defects, leading to enhanced crystallinity. This is also ascertained from the Pb^{2+} 4f peak shift and reduced metallic Pb^0 peak observed in XPS spectra of TAEA containing the FACs film shown in Fig. 7a.

TAEA is a large sized molecule and hence cannot fit into the voids of the $[PbI_6]^{4-}$ polyhedral frame. Therefore, it is highly likely that TAEA is not substituting the A-site cations in the $FA_{0.83}Cs_{0.17}Pb(I_{0.90}Br_{0.10})_3$ lattice and lies on the surface. Water contact angle measurements shown in Fig. 6c–g show an increase in the contact angle with an increase in the concentration of TAEA in the perovskite precursor, which signifies the increased hydrophobicity of the surface with increased TAEA concentrations. So, the possibility of the presence of TAEA on the surface is very high, which makes the surface more resistant to water ingress and thus provides a rational explanation for the enhanced ambient stability.

The amino groups in TAEA ($-NH_2$) can coordinate with metal cations such as Pb^{2+} in the perovskite structure. This can involve the formation of coordination bonds between the nitrogen atoms of the amino groups and the metal cations as shown in the schematic shown in Fig. 8a. It is previously reported that $-NH_2$ containing additives tend to form N–H···X hydrogen bonds (H-bonds) with the halides in the perovskite structure (I and Br).[54] This strong interaction between $-NH_2$ and the halide, suppresses I^- ion migration as shown by the schematic in Fig. 8a. Ion migration can lead to the creation of defects and degradation of the crystal structure. Thermal decomposition of the perovskite can occur, especially in the presence of moisture and oxygen. High-quality, defect-free films with well-defined crystal structures are more stable under thermal stress. Due to the longer bond length of TAEA it can cross-link the two adjacent perovskite units on the surface making H-bonds with the halides. Therefore, two branches of TAEA may bond with the surface of FACs perovskite and the third is protruding out of the surface as shown in Fig. 8a.

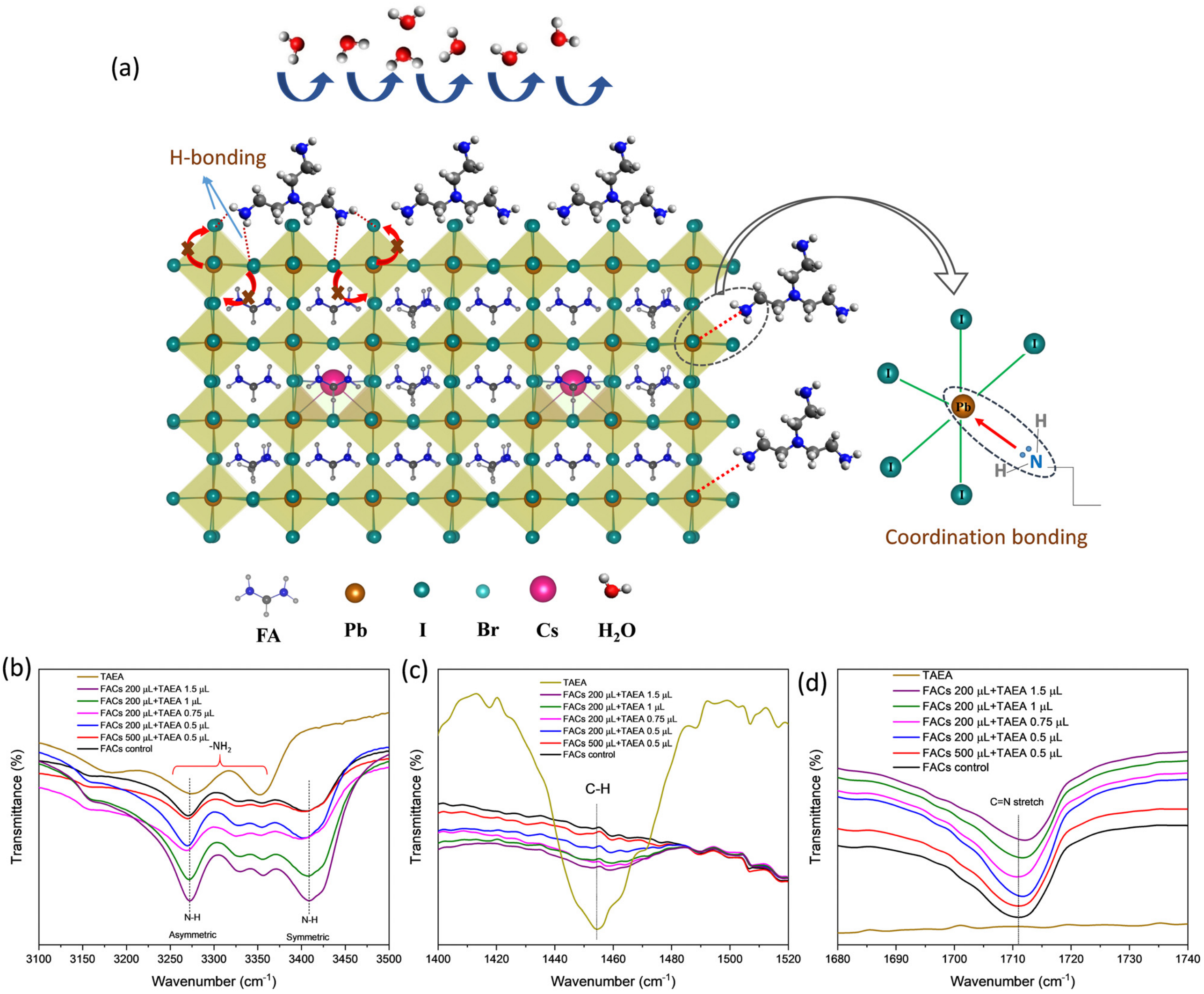

Fig. 8 (a) Schematic showing the interaction of TAEA with the FACs lattice. FTIR spectra showing the TAEA and FACs perovskite film containing different concentrations of TAEA showing (b) N–H stretching, (c) C–H stretching, and (d) C=N stretching.

Therefore, TAEA can act as a protective layer, shielding the perovskite from moisture and oxygen, which are known to cause degradation in perovskite materials. This protection is essential for retaining the α-phase at room temperature and highly humid conditions for the long term as observed from the degradation studies shown in Fig. 6a, b and Fig. S2, S4 (ESI†).

To trace the interaction between TAEA and FACs perovskite lattice, Fourier Transform Infrared spectroscopy (FTIR) was performed as shown in Fig. 8b–d. FTIR spectra of TAEA presented in Fig. 8b show broad peaks in the range 3200–3400 cm^{-1} corresponding to the $-NH_2$ vibrational modes. FTIR peaks corresponding to N–H stretching are detected in all the FACs films. FTIR peaks in FACs films at 3270 cm^{-1} and 3408 cm^{-1} are associated with the asymmetric and symmetric stretching vibrations of the N–H bond of FA^+, respectively.[55] An increase in the TAEA concentration leads to the broadening of the peak and an increase in the peak intensity, which could account for the H-bond formation between the $-NH_2$ in TAEA with the perovskite lattice.[56] The FTIR peak at around 1458 cm^{-1} shown in Fig. 8c corresponds to the stretching due to the C–H bond in TAEA. This peak is not present in the control FACs film, however, as we go on increasing the concentration of TAEA in FACs this peak starts to appear. It again validates the fact that TAEA has bonded with the perovskite and is present in the film. The peak intensity is greatly reduced with the incorporation of TAEA in the FACs film, owing to the interaction between TAEA and the FACs lattice. The characteristic FTIR peak near 1711 cm^{-1} corresponds to the $C{=}N$ stretching present due to the presence of FA^+. This stretching is not present in TAEA as shown in Fig. 8d. However, when TAEA is added into the FACs perovskite this peak is shifted which hints towards interaction between the FA^+ and TAEA. The hydrogen atom from the amino group in TAEA can form a hydrogen bond with the nitrogen atom of the amide group in FA. The hydrogen atom is attracted to the lone pair of electrons on the nitrogen atom, creating a hydrogen bond. This bonding can suppress the volatilization of FA from perovskite and further improve the stability.

Conclusions

In summary, we have presented a systematic study of the effect of different concentrations of TAEA on the FACs-based perovskite. The incorporation of TAEA in the FACs precursor has led to enhanced structural, absorbance, and optoelectronic properties. The optimum concentration of TAEA in FACs is found to be 1 μL in 200 μL. TAEA incorporation results in reduced pinholes and hence yields a compact, smother, and uniform morphology. TAEA containing FACs films are stable for more than 180 days in a highly humid and illuminated ambient environment, whereas the pristine FACs begins to degrade within 110 days of exposure. The incorporation of TAEA in FACs films has also led to a drastic enhancement in thermal stability. TAEA containing FACs films are stable for more than 7 days under continuous exposure to extreme conditions of high humidity, illumination, and thermal stress at 85 °C. So, this study provides a scientific approach for long-term stabilization of the most commonly studied and promising mixed cation FACs perovskite composition, paving the way for its mass commercialization as an efficient and long run stable perovskite technology.

Experimental section

Materials and methods

Chemicals and reagents. Cesium iodide (CsI, 99.9%), dimethyl sulfoxide (DMSO, anhydrous, 99.8%), and *N*,*N*-dimethylformamide (DMF, anhydrous, 99.8%) were purchased from Sigma-Aldrich. Lead iodide (PbI_2, 99.99%), lead bromide ($PbBr_2$, >98.0%), and Tris(2-aminoethyl)amine (TAEA, >98.0%) were purchased from TCI. Formamidinium iodide (FAI, >99.99%) was purchased from Greatcellsolar Materials. All salts and solvents were used as received without any further purification.

Perovskite precursor solutions preparation. The precursor for $FA_{0.83}Cs_{0.17}Pb(I_{0.90}Br_{0.10})_3$ (denoted as FACs) films were prepared by adding 64 mg of CsI, 207 mg of FAI, 80 mg of $PbBr_2$, and 568 mg of PbI_2 to 1 mL of the mixture of DMF and DMSO in a volumetric ratio of 4 : 1. The precursor solution was stirred for 15 min at 70 °C prior to deposition. TAEA was added into $FA_{0.83}Cs_{0.17}Pb(I_{0.90}Br_{0.10})_3$ precursor in different volume-by-volume ratios of $FA_{0.83}Cs_{0.17}Pb(I_{0.90}Br_{0.10})_3$/TAEA (500 μL : 0.5 μL, 200 μL : 0.5 μL, 200 μL : 0.75 μL, 200 μL : 1 μL, and 200 μL : 1.5 μL) and shaken vigorously on a shaker for a couple of hours to obtain a clear solution.

Perovskite film deposition. Glass slides were cleaned sequentially with labolene solution followed by ultra-sonication in de-ionized water, acetone, and IPA respectively. The glass slides were then treated in the oxygen plasma cleaning chamber for 10 min. The precursors were coated on the cleaned slides at 5000 rpm for 35 s in a N_2 filled glovebox. Films were annealed at 100 °C for 20 minutes. All the films were then exposed to ambient conditions with RH ∼ 60–70% for stability studies.

Characterizations. UV-Vis absorption measurements were conducted using a PerkinElmer Lambda 1050 spectrophotometer. X-ray diffraction (XRD) measurements were carried out using a Rigaku Ultima IV diffractometer for structural analysis at a scan speed of 3° per minute and step size of 0.02° using a CuKα target. Steady-state Photoluminescence (PL) was measured using a Shimadzu RF-5000 fluorescence spectrophotometer to examine the photoactivity of the samples. Surface morphology and EDS mapping were observed using field emission scanning electron microscopy (FESEM) JEOL JSM-7800F Prime high-resolution SEM. Spatial PL intensity maps were recorded using a FLOWVIEW FV 1200 scanning laser confocal microscope system. BRUKER-DIMENSION ICON AFM was used to study the surface topography. PL mapping and AFM analysis were carried out using FiJi and Gwyddion free software. X-ray photoelectron spectroscopy (XPS) was also carried out using an AXIS Supra instrument by using a monochromatized Al Kα source ($h\nu$ = 1486.6 eV).

Conflicts of interest

The authors declare no competing financial interest.

Acknowledgements

The authors would like to acknowledge the Department of Science and Technology, India for providing funding. P. C. acknowledges IIT Delhi for providing Senior Research Fellowship. We would also like to acknowledge Nanoscale Research Facility (NRF) and Central Research Facility (CRF) at the Indian Institute of Technology, Delhi for characterization measurements.

Notes and references

1 C. C. Stoumpos, C. D. Malliakas and M. G. Kanatzidis, *Inorg. Chem.*, 2013, **52**, 9019–9038.
2 S. D. Stranks, G. E. Eperon, G. Grancini, C. Menelaou, M. J. P. Alcocer, T. Leijtens, L. M. Herz, A. Petrozza and H. J. Snaith, *Science*, 1979, **342**, 341–344.
3 A. Miyata, A. Mitioglu, P. Plochocka, O. Portugall, J. T. W. Wang, S. D. Stranks, H. J. Snaith and R. J. Nicholas, *Nat. Phys.*, 2015, **11**, 582–587.
4 National Renewable Energy Laboratory NREL. Best-Research Cell-Efficiencies, 2023.
5 T. A. Berhe, W. N. Su, C. H. Chen, C. J. Pan, J. H. Cheng, H. M. Chen, M. C. Tsai, L. Y. Chen, A. A. Dubale and B. J. Hwang, *Energy Environ. Sci.*, 2016, **9**, 323–356.
6 B. Conings, J. Drijkoningen, N. Gauquelin, A. Babayigit, J. D'Haen, L. D'Olieslaeger, A. Ethirajan, J. Verbeeck, J. Manca, E. Mosconi, F. De Angelis and H. G. Boyen, *Adv. Energy Mater.*, 2015, **15**, 1500477.
7 A. Rana, P. Sharma, A. Kumar, S. Pareek, S. Waheed, R. K. Singh and S. Karak, *IEEE Trans. Electron Devices*, 2021, **68**, 3907–3913.
8 M. Bag, L. A. Renna, R. Y. Adhikari, S. Karak, F. Liu, P. M. Lahti, T. P. Russell, M. T. Tuominen and D. Venkataraman, *J. Am. Chem. Soc.*, 2015, **137**, 13130–13137.
9 B. P. Dhamaniya, P. Chhillar, B. Roose, V. Dutta and S. K. Pathak, *ACS Appl. Mater. Interfaces*, 2019, **25**, 22228–22239.
10 P. Chhillar, B. P. Dhamaniya, V. Dutta and S. K. Pathak, *ACS Omega*, 2019, **4**, 11880–11887.
11 J. W. Lee, D. J. Seol, A. N. Cho and N. G. Park, *Adv. Mater.*, 2014, **26**, 4991–4998.
12 G. E. Eperon, S. D. Stranks, C. Menelaou, M. B. Johnston, L. M. Herz and H. J. Snaith, *Energy Environ. Sci.*, 2014, **7**, 982–988.
13 C. C. Stoumpos, C. D. Malliakas and M. G. Kanatzidis, *Inorg. Chem.*, 2013, **52**, 9019–9038.
14 N. J. Jeon, J. H. Noh, W. S. Yang, Y. C. Kim, S. Ryu, J. Seo and S. Il Seok, *Nature*, 2015, **517**, 476–480.
15 A. Binek, F. C. Hanusch, P. Docampo and T. Bein, *J. Phys. Chem. Lett.*, 2015, **6**, 1249–1253.
16 N. Pellet, P. Gao, G. Gregori, T. Y. Yang, M. K. Nazeeruddin, J. Maier and M. Grätzel, *Angew. Chem., Int. Ed.*, 2014, **53**, 3151–3157.
17 T. Leijtens, G. E. Eperon, N. K. Noel, S. N. Habisreutinger, A. Petrozza and H. J. Snaith, *Adv. Energy Mater.*, 2015, **5**, 1500963.
18 F. Yao, P. Gui, C. Chen, B. Li, R. Li, C. Tao, Q. Lin and G. Fang, *ACS Appl. Mater. Interfaces*, 2019, **11**, 39875–39881.
19 R. Chen, Y. Wu, Y. Wang, R. Xu, R. He, Y. Fan, X. Huang, J. Yin, B. Wu, J. Li and N. Zheng, *Adv. Funct. Mater.*, 2021, **11**, 2008760.
20 M. Abdi-Jalebi, Z. Andaji-Garmaroudi, A. J. Pearson, G. Divitini, S. Cacovich, B. Philippe, H. Rensmo, C. Ducati, R. H. Friend and S. D. Stranks, *ACS Energy Lett.*, 2018, **3**, 2671–2678.
21 J. W. Lee, D. H. Kim, H. S. Kim, S. W. Seo, S. M. Cho and N. G. Park, *Adv. Energy Mater.*, 2015, **5**, 1501310.
22 S. Masi, A. F. Gualdrón-Reyes and I. Mora-Seró, *ACS Energy Lett.*, 2020, **5**, 1974–1985.
23 S. Maniyarasu, J. C.-R. Ke, B. F. Spencer, A. S. Walton, A. G. Thomas and W. R. Flavell, *ACS Appl. Mater. Interfaces*, 2021, **13**, 43573–43586.
24 D. P. Mcmeekin, G. Sadoughi, W. Rehman, G. E. Eperon, M. Saliba, M. T. Hörantner, A. Haghighirad, N. Sakai, L. Korte, B. Rech, M. B. Johnston, L. M. Herz and H. J. Snaith, *Science*, 2016, **351**, 151–155.
25 Y. Hu, E. M. Hutter, P. Rieder, I. Grill, J. Hanisch, M. F. Aygüler, A. G. Hufnagel, M. Handloser, T. Bein, A. Hartschuh, K. Tvingstedt, V. Dyakonov, A. Baumann, T. J. Savenije, M. L. Petrus and P. Docampo, *Adv. Energy Mater.*, 2018, **8**, 1703057.
26 J. Yang, X. Liu, Y. Zhang, X. Zheng, X. He, H. Wang, F. Yue, S. Braun, J. Chen, J. Xu, Y. Li, Y. Jin, J. Tang, C. Duan, M. Fahlman and Q. Bao, *Nano Energy*, 2018, **54**, 218–226.
27 F. X. Liang, J. Z. Wang, Z. X. Zhang, Y. Y. Wang, Y. Gao and L. B. Luo, *Adv. Opt. Mater.*, 2017, **22**, 1700654.
28 P. Chhillar, B. P. Dhamaniya, S. K. Pathak and S. Karak, *ACS Appl Electron. Mater.*, 2022, **4**, 5368–5378.
29 K. Wang, Z. Jin, L. Liang, H. Bian, H. Wang, J. Feng, Q. Wang and S. (Frank) Liu, *Nano Energy*, 2019, **58**, 175–182.
30 H. Zhao, J. Xu, S. Zhou, Z. Li, B. Zhang, X. Xia, X. Liu, S. Dai and J. Yao, *Adv. Funct. Mater.*, 2019, **27**, 1808986.
31 B. Zhao, S. F. Jin, S. Huang, N. Liu, J. Y. Ma, D. J. Xue, Q. Han, J. Ding, Q. Q. Ge, Y. Feng and J. S. Hu, *J. Am. Chem. Soc.*, 2018, **140**, 11716–11725.
32 R. J. Sutton, M. R. Filip, A. A. Haghighirad, N. Sakai, B. Wenger, F. Giustino and H. J. Snaith, *ACS Energy Lett.*, 2018, **3**, 1787–1794.
33 N. K. Cho, H. J. Na, J. Yoo and Y. S. Kim, *Commun. Mater.*, 2021, **1**, 30.
34 W. Zhu, A. A. Khan, M. M. Rana, R. Gautheron-Bernard, N. R. Tanguy, N. Yan, P. Turban, S. Ababou-Girard and D. Ban, *ACS Omega*, 2022, **7**, 10559–10567.
35 A. Marronnier, G. Roma, S. Boyer-Richard, L. Pedesseau, J. M. Jancu, Y. Bonnassieux, C. Katan, C. C. Stoumpos,

M. G. Kanatzidis and J. Even, *ACS Nano*, 2018, **12**, 3477–3486.

36 A. K. Jena, A. Kulkarni, Y. Sanehira, M. Ikegami and T. Miyasaka, *Chem. Mater.*, 2018, **30**, 6668–6674.

37 G. E. Eperon, G. M. Paternò, R. J. Sutton, A. Zampetti, A. A. Haghighirad, F. Cacialli and H. J. Snaith, *J. Mater. Chem. A Mater.*, 2015, **3**, 19688–19695.

38 J. Tian, Q. Xue, Q. Yao, N. Li, C. J. Brabec and H. L. Yip, *Adv. Energy Mater.*, 2020, 10.

39 Y. Wang, J. Song, J. Ye, Y. Jin, X. Yin, Z. Su, L. Hu, Y. Wu, C. Qiu, H. Wang, W. Yan and Z. Li, *Chem. Commun.*, 2023, **43**, 6580–6583.

40 Z. Wang, Q. Lin, F. P. Chmiel, N. Sakai, L. M. Herz and H. J. Snaith, *Nat. Energy*, 2017, **9**, 1–10.

41 D. Vaitukaityte, Z. Wang, T. Malinauskas, A. Magomedov, G. Bubniene, V. Jankauskas, V. Getautis and H. J. Snaith, *Adv. Mater.*, 2018, **45**, 1803735.

42 W. Rehman, D. P. McMeekin, J. B. Patel, R. L. Milot, M. B. Johnston, H. J. Snaith and L. M. Herz, *Energy Environ. Sci.*, 2017, **10**, 361–369.

43 G. Murugadoss, P. Arunachalam, S. K. Panda, M. Rajesh Kumar, J. R. Rajabathar, H. Al-Lohedan and M. D. Wasmiah, *J. Mater. Res. Technol.*, 2021, **12**, 1924–1930.

44 X. Ding, H. Chen, Y. Wu, S. Ma, S. Dai, S. Yang and J. Zhu, *J. Mater. Chem. A Mater.*, 2018, **6**, 18258–18266.

45 Y. Jiang, J. Yuan, Y. Ni, J. Yang, Y. Wang, T. Jiu, M. Yuan and J. Chen, *Joule*, 2018, **2**, 1356–1368.

46 F. Li, Y. Pei, F. Xiao, T. Zeng, Z. Yang, J. Xu, J. Sun, B. Peng and M. Liu, *Nanoscale*, 2018, **10**, 6318–6322.

47 K. Wang, Z. Li, F. Zhou, H. Wang, H. Bian, H. Zhang, Q. Wang, Z. Jin, L. Ding and S. Liu, *Adv. Energy Mater.*, 2019, **42**, 1902529.

48 F. Li, X. Deng, F. Qi, Z. Li, D. Liu, D. Shen, M. Qin, S. Wu, F. Lin, S. H. Jang, J. Zhang, X. Lu, D. Lei, C. S. Lee, Z. Zhu and A. K. Y. Jen, *J. Am. Chem. Soc.*, 2020, **142**, 20134–20142.

49 Y. Zhang and N. G. Park, *ACS Energy Lett.*, 2022, **7**, 757–765.

50 F. Zhang, J. Song, B. Cai, X. Chen, C. Wei, T. Fang and H. Zeng, *Sci. Bull.*, 2021, **66**, 2189–2198.

51 M. Li, R. Sun, J. Chang, J. Dong, Q. Tian, H. Wang, Z. Li, P. Yang, H. Shi, C. Yang, Z. Wu, R. Li, Y. Yang, A. Wang, S. Zhang, F. Wang, W. Huang and T. Qin, *Nat. Commun.*, 2023, **14**, 573.

52 W.-Q. Wu, Z. Yang, P. N. Rudd, Y. Shao, X. Dai, H. Wei, J. Zhao, Y. Fang, Q. Wang, Y. Liu, Y. Deng, X. Xiao, Y. Feng and J. Huang, *Science*, 2019, **5**, eaav8925.

53 X. Hou, S. Huang, W. Ou-Yang, L. Pan, Z. Sun and X. Chen, *ACS Appl. Mater. Interfaces*, 2017, **9**, 35200–35208.

54 W. Feng, Y. Tan, M. Yang, Y. Jiang, B. X. Lei, L. Wang and W. Q. Wu, *Chem*, 2022, **8**, 351–383.

55 X. He, T. Wu, X. Liu, Y. Wang, X. Meng, J. Wu, T. Noda, X. Yang, Y. Moritomo, H. Segawa and L. Han, *J. Mater. Chem. A Mater.*, 2020, **8**, 2760–2768.

56 I. Zojaji, A. Esfandiarian and J. Taheri-Shakib, *Adv. Colloid Interface Sci.*, 2021, **289**, 102314.